

Article

Interactions between a H₂ Molecule and Carbon Nanostructures: A DFT Study

Dominik Gehringer ^{1,*}, Thomas Dengg ², Maxim N. Popov ²  and David Holec ¹ 

¹ Department of Materials Science, Montanuniversität Leoben, Franz-Josef-Straße 18, A-8700 Leoben, Austria; david.holec@unileoben.ac.at

² Materials Center Leoben Forschung GmbH, Roseggerstraße 12, A-8700 Leoben, Austria; thomas.dengg@protonmail.com (T.D.); maxim.popov@mcl.at (M.N.P.)

* Correspondence: dominik.gehringer@unileoben.ac.at

Received: 24 February 2020; Accepted: 18 March 2020; Published: 24 March 2020



Abstract: On a long path of finding appropriate materials to store hydrogen, graphene and carbon nanotubes have drawn a lot of attention as potential storage materials. Their advantages lie at hand since those materials provide a large surface area (which can be used for physisorption), are cheap compared to metal hydrides, are abundant nearly everywhere, and most importantly, can increase safety to existing storage solutions. Therefore, a great variety of theoretical studies were employed to study those materials. After a benchmark study of different van-der-Waals corrections to Generalized Gradient Approximation (GGA), the present Density Functional Theory (DFT) study employs Tkatchenko–Scheffler (TS) correction to study the influence of vacancy and Stone–Wales defects in graphene on the physisorption of the hydrogen molecule. Furthermore, we investigate a large-angle (1,0) grain boundary as well as the adsorption behaviour of Penta-Octa-Penta (POP)-graphene.

Keywords: hydrogen storage; physisorption; Density Functional Theory; van der Waals correction; carbon nanostructures; defects

1. Introduction

On the quest for environmentally-friendly energy generation, chemical energy released during formation of a water molecule out of hydrogen atoms reacting with atmospheric oxygen has been proposed as a possible route. For any practical usage, however, it is critical to solve a question of storing hydrogen. The currently available technology using high-pressure tanks is too risky for, e.g., automobile applications, and therefore alternative solutions are needed. Here, carbon-based nano-structured materials have been suggested as promising candidates for hydrogen storage [1]. In fact, it was the discoverers [2] of graphene themselves, who first showed that the novel 2D material could store hydrogen easily at cryogenic temperatures and release it again at higher temperatures [3]. Consequently, the adsorption properties of pristine graphene [4–9] were extensively studied previously both experimentally as well as theoretically. In order to tune the material response further, chemical as well as structural modifications to graphene can be introduced. These include, e.g., metal decoration [10–13] or application of perforated graphene [14,15]. The present study thus focuses on the latter area which has not been thoroughly explored yet. In doing so, we consider impact of structural defects on the local adsorption properties and try to extract simple rule-of-thumb guidelines which can be used to steer further optimization of the carbon-based materials for H₂ storage.

Namely, we investigated a single vacancy and a Stone–Wales defect [16,17] as examples for point defects. As a more complex structural line defect, we considered also an energetically favorable [18] symmetric large angle grain boundary composed of (1,0) dislocations. Such defects in graphene were

studied before with respect to their impact on mechanical or electronic properties [18–22], here we newly present their impact on the H₂ adsorption capacity of graphene. Based on the results obtained from the (1,0) grain boundary we furthermore investigated Penta-Octa-Penta (POP-)graphene as a graphene modification containing no hexagons, which was theoretically predicted by Wang et al. and proposed to be a promising candidate for lithium-ion batteries [23].

All our calculations include an impact of long-range dispersion (van-der-Waals) forces as an add-on to standard density functional theory calculations using Tkatchenko–Scheffler (TS) method [24]. As this method is not (yet) widely employed, we started with a benchmark study of the hydrogen adsorption on pristine graphene, whereby we could compare our data with literature data [4], which provides a useful reference for any future studies using TS method.

Finally, in order to explain the different adsorption behavior of the studied structural defects, we implemented the TS method using the *SciPy* [25,26] stack, by which we can demonstrate that the changes in electronic structure result in only minor contributions to the van-der-Waals-like interactions.

2. Computational Methods

All quantum-mechanical calculations were carried out with the Vienna Ab-initio Simulation Package (VASP) [27,28]. The exchange and correlation functional was treated at generalized gradient approximation level parametrised by Perdew–Burke–Ernzerhof (PBE-GGA) [29,30]. The projector augmented wave (PAW) method [31,32] was used to describe the electron-ion interactions. The used cutoff energy of the plane-wave basis set was tested for convergence of the total energy to ≈ 0.1 meV/at. The tests were carried out by employing Γ -centred *k*-mesh sampling of the Brillouin zone for hexagonal cells (graphene), and Monkhorst-Pack [33] mesh for rectangular cells. The meshes used in the present study are summarized in Table 1. In order to take into account also the van-der-Waals interaction, various dispersion correction methods (DFT-D2 [34], DFT-D3 [35], DFT-TS [24,36]) implemented in VASP were tested for their ability to reproduce experimental lattice parameters of graphite and graphene. The results of the benchmark study are shown in Table A1. Based on these results, all subsequent geometric optimizations were performed using the Tkatchenko-Scheffler (DFT-TS) method, performance of which was assessed already in various previous studies for carbon structures [37–39]. Geometric optimizations were carried out by employing a conjugate gradient algorithm with an energy convergence criterion of 10^{-4} eV (per simulation box). The energy convergence criterion for self-consistency of the electronic loop was set 10^{-6} eV (per simulation box). To minimize periodic-boundary image interactions we used a 25 Å vacuum layer along the *c* axis for all cells, as well as a $5 \times 5 \times 1$ supercell of a standard 2-atom graphene unit cell.

Table 1. *k*-meshes used for sampling the Brillouin zone.

System	<i>k</i> -Mesh Type	<i>k</i> -Mesh	Supercell
graphene	Γ -centered	$5 \times 5 \times 1$	$5 \times 5 \times 1$
single vacancy	Γ -centered	$5 \times 5 \times 1$	$5 \times 5 \times 1$
Stone–Wales defect	Γ -centered	$5 \times 5 \times 1$	$5 \times 5 \times 1$
(1,0) grain boundary	Monkhorst-Pack	$7 \times 10 \times 1$	
POP-graphene	Monkhorst-Pack	$5 \times 9 \times 1$	

2.1. Graphene Adsorption Curves

In order to study the adsorption of the H₂ molecule, the hydrogen molecule was placed in different alignments on three different adsorption sites (Figure 1). Directly above a carbon atom, hereafter referred to as a *top* site, above a bond between two carbon atoms (a *bridge* site) and above the centre of a hexagon (a *hexagon* site). In the *x*(*y*)-alignment, the H₂ molecule longitudinal axis is parallel(perpendicular) to the *a* lattice vector, while in the *v*-alignment the molecule is parallel to the *c* lattice vector of the simulation cell. Here we note that all other papers just examine only 6 different configurations [4,40–42], corresponding to the three adsorption sites and *x* and *v*-alignments.

Indeed, also our calculations show that the x and y alignments yield identical results, and therefore hereafter we present them as h-alignment. We also note that our setup could, in principle, provide also information as a function of rotational degree of freedom similar to, e.g., Ref. [43]. However, in the case of the adsorption maps being investigated here, such procedure becomes computationally prohibitive and hence we stick to one special alignment. For each of the resulting 9 H_2 configurations, the following procedure was applied:

1. Fully relax the position and geometry of the H_2 molecule, while keeping the C atoms in the graphene plane fixed.
2. Vary the height of the molecule with fixed geometry above the graphene sheet ranging from 2 Å to 12 Å.
3. Calculate the interaction energy $E_{int,graphene+H_2}$ as:

$$E_{int,graphene+H_2} = E_{tot,graphene+H_2} - E_{tot,graphene} - E_{tot,H_2}(d_{case}) \quad (1)$$

where d_{case} refers to the bond-length obtained from the full relaxation of the molecule. The energy for the hydrogen molecule $E_{tot,H_2}(d_{case})$ with bond-length of $d_{case} = 0.75$ Å, which corresponds to the theoretical equilibrium bond-length, was obtained from a separate calculation. Therefore, the two H atoms of an isolated H_2 molecule were separated, while for each separation the total energy $E_{tot,H_2}(d_{case})$ was calculated. To obtain consistent results we employed DFT-TS correction, with a Γ -point only k -mesh to avoid interactions originating from periodic boundary conditions.

In the following paragraphs, E_{ads} refers to the minimum of the interaction energy curve $E_{int}(h_{ads})$, where the height above the graphene plane, h_{ads} , denotes the vertical distance between graphene and the center of mass of the H_2 molecule.

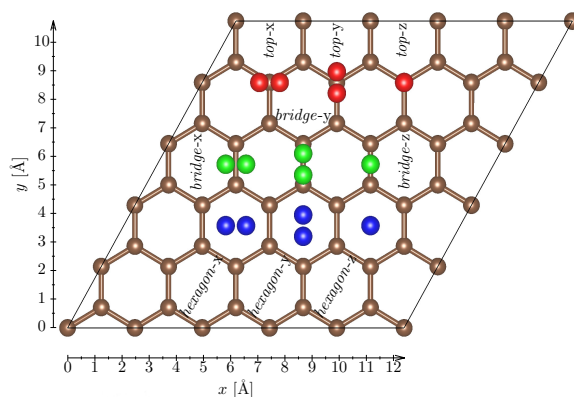


Figure 1. Schematic view of different (high-symmetry) sites for placing hydrogen molecule on graphene (top-red configurations, bridge-green configurations and hexagon-blue configurations).

2.2. Adsorption Maps

All adsorption maps shown in this work have been calculated with z -direction (perpendicular to the graphene plane) H_2 molecule alignment, in order to provide data which is comparable to literature. In order to minimize computational effort, only an irreducible wedge of the supercell was sampled for each system and subsequently unfolded to span the whole supercell (see Table 2). For each sampling point, adsorption energy was calculated for at least 7 different molecule heights around the expected minimum, and fitted with a cubic fit in order to obtain the corresponding adsorption energy and height. Figure 3 shows clips of the calculated adsorption maps.

Table 2. Parameters of the sampling used for constructing the adsorption maps. Sampling lattice refers to the symmetry of the sampling lattice, irreducible wedge defines the directions enclosing the sampling area. Symmetry operations refer to how the irreducible wedge is unfolded in order to sample the whole supercell lattice.

System	Supercell Lattice	Sampling Lattice	Irreducible Wedge	Samples	Symmetry Operations
graphene	$a = b = 12.35 \text{ \AA}$ hexagonal	hexagonal	$[1\ 0\ 0], [0\ 1\ 0]$	121	
single vacancy	$a = b = 12.35 \text{ \AA}$ hexagonal	triangle	$[1\ 1\ 0], [1\ \bar{2}\ 0]$	66	$\underbrace{3}_{[0\ 0\ 1]} \underbrace{m}_{\{1\ \bar{2}\ 0\}}$
Stone–Wales defect	$a = b = 12.35 \text{ \AA}$ hexagonal	hexagonal (rotated by 30° with respect to the supercell lattice)	$[1\ 1\ 0], [\bar{1}\ 1\ 0]$	110	$\underbrace{m}_{\{1\ 1\ 0\}} \underbrace{m}_{\{\bar{1}\ 1\ 0\}}$
(1,0) grain boundary	$a = 22.66 \text{ \AA},$ $b = 6.54 \text{ \AA}$ orthorhombic	rectangular	$[1\ 0\ 0], [0\ 1\ 0]$	170	$\underbrace{m}_{\{1\ 0\ 0\}} \underbrace{m}_{\{0\ 1\ 0\}}$
POP-graphene	$a = 11.05 \text{ \AA},$ $b = 9.09 \text{ \AA}$ orthorhombic	rectangular	$[1\ 0\ 0], [0\ 1\ 0]$	285	$\underbrace{m}_{\{1\ 0\ 0\}} \underbrace{m}_{\{0\ 1\ 0\}}$

3. Results

3.1. Hydrogen Adsorption on Pristine Graphene

As mentioned above, we start with testing the DFT-TS method against literature data, which was obtained by employing Grimme’s D3 method (DFT-D3). Similarly to the previous works [4,8,40–42,44], we consider 3 high-symmetry adsorption sites (*hexagon*—centre of a hexagon, *top*—above a C atom, *bridge*—above a C–C bond), with both horizontal and vertical molecule alignment. The results for H₂ physisorption on pristine graphene are summarized in Table 3 and the complete adsorption curves are shown Figure 2. Our E_{ads} values are in good agreement with previous works [4,42], however our work suggests the *hexagon*-h alignment to be the most favorable in contrast to the *hexagon*-v geometries reported previously. We note that also the equilibrium adsorption heights are in reasonable agreement between the DFT-TS (used in the present study) and DFT-D3 employed previously [41,42], except for the *hexagon*-h arrangement. Here, the DFT-TS yields somewhat tighter binding (2.94 Å compared to 3.10 Å for the DFT-D3 method), as well as a stronger adsorption tendency. The same study was also carried out for POP-graphene, with in total nine adsorption sites (Figure A1). The corresponding results are shown in Figure A2.

Table 3. Adsorption energies of the H₂ molecule on the three adsorption sites in all here considered configurations (see Figure 1, x- and y-alignments yield the same behaviour and are labelled h). DFT-PBE-D3 values are taken from Ref. [4].

Configuration		DFT-PBE-TS		DFT-PBE-D3 [4]	
Site	Alignment	E_{ads} [meV]	h_{ads} [Å]	E_{ads} [meV]	h_{ads} [Å]
<i>hexagon</i>	v	−69	3.15	−69	3.10
<i>bridge</i>	v	−63	3.19	−63	3.18
<i>top</i>	v	−62	3.19	−63	3.18
<i>hexagon</i>	h	−75	2.94	−67	3.10
<i>bridge</i>	h	−63	3.09	−58	3.16
<i>top</i>	h	−62	3.10	−57	3.16

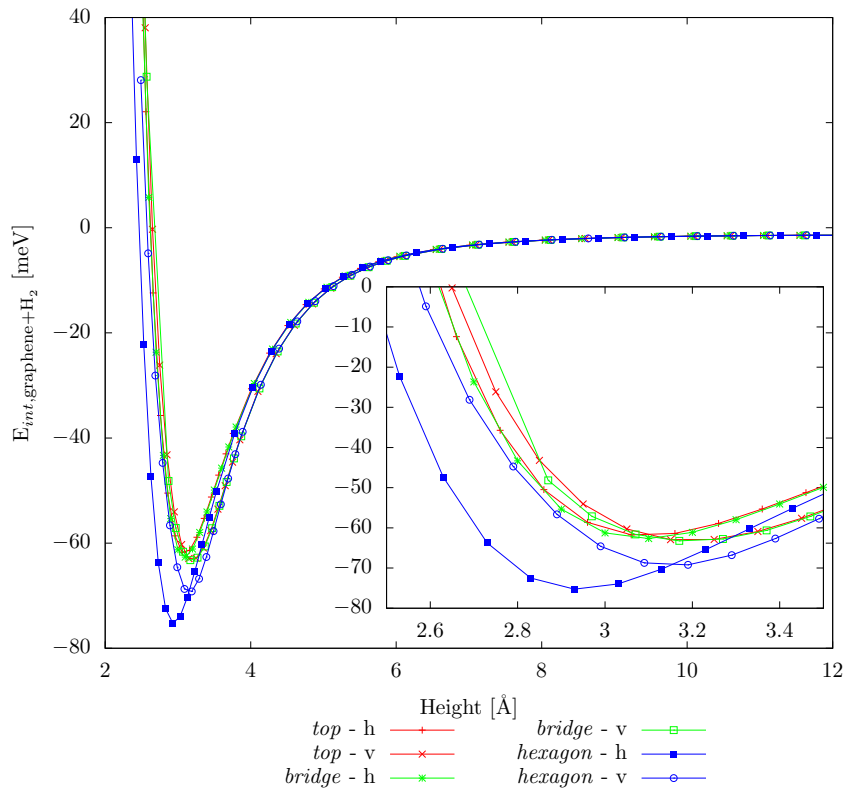


Figure 2. Interaction energy, E_{int} , for two different alignments (horizontal, h, and vertical, v) of the H_2 molecule at three adsorption sites (*top*, *bridge*, *hexagon*) on graphene.

3.2. Adsorption Maps and Pristine Graphene

The main focus of the present work is to investigate the role of defects on the adsorption properties. The adsorption maps were obtained for the H_2 molecule in *hexagon-v* configuration (cf. Section 2.2). Figure 3 shows only $10 \times 10 \text{ \AA}^2$ clips of the calculated supercells, for the full adsorption maps we refer the reader to the supplementary material. The color-code and the contour lines refer to the adsorption energy and are consistent throughout the whole manuscript to allow for an easy comparison between different adsorption scenarios in various figures.

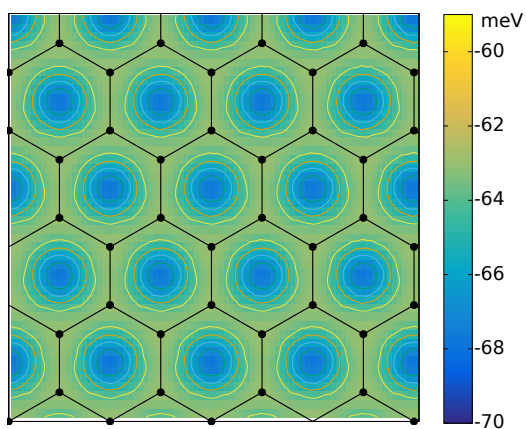
As a measure to quantify the adsorption capacity improvement compared with pristine graphene, we used the fraction of the adsorption area which exhibits more negative adsorption energy (i.e., stronger physisorption) than the minimum of graphene:

$$f = \frac{1}{A} \int_A p(\mathbf{r}) d^2\mathbf{r}, \quad p(\mathbf{r}) = \begin{cases} 1 & \text{if } E_{ads}(\mathbf{r}) \leq \min(E_{ads,graphene}) = -68.7 \text{ meV}, \\ 0 & \text{otherwise,} \end{cases} \quad (2)$$

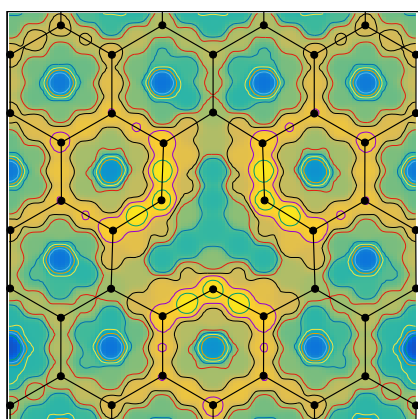
where A is the adsorption area per supercell. This quantification is motivated by one of the main graphene advantages, namely its vast surface area, which is also relevant for other carbon nanostructures. The adsorption area is expected to correlate with the hydrogen storage capacity. Nevertheless, the area with strong adsorption capability (at 0 K, see last column in Table 4) is only one of the parameters influencing the adsorption capacity. For example, external parameters such as temperature or pressure, or interaction with other H_2 molecules are also influencing the overall H_2 uptake, and thus we refrain from its direct relation to the hydrogen storage capacity.

As a first step, we evaluated the adsorption energy, E_{ads} , for the pristine graphene supercell in order to get a reference value for comparison. According to Table 3 and Figure 2 the adsorption map (Figure 3a) clearly shows that the minimum of the adsorption energy is in the center of hexagon,

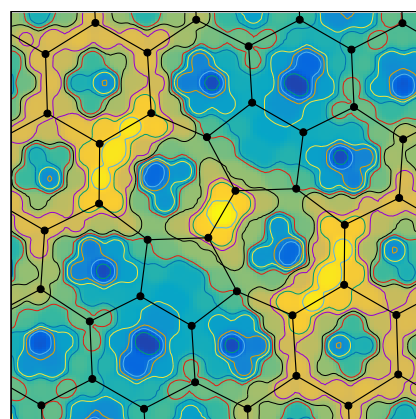
while the absolute value around bonds (*bridge sites*) and carbons atoms (*top sites*) exhibits a weaker interaction (difference ≈ 6 meV/H₂).



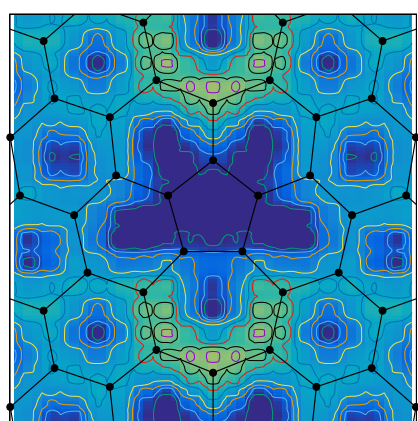
(a) adsorption map of pristine graphene



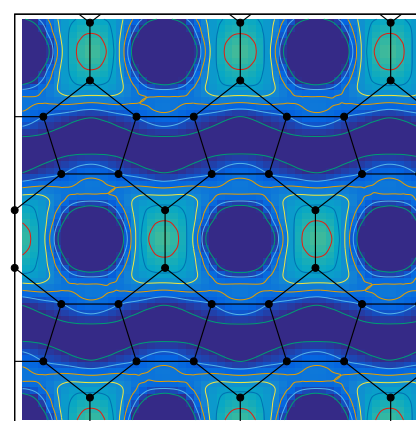
(b) adsorption map of graphene with a single vacancy defect



(c) adsorption map of graphene with a Stone-Wales defect



(d) adsorption map of graphene with a symmetric (1,0) grain boundary



(e) adsorption map of pop graphene

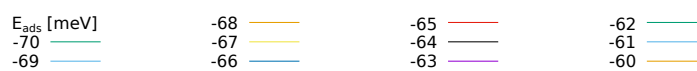


Figure 3. Adsorption maps of various graphene variants. The figures (a–e) are all 10×10 Å clips of the sampled supercells.

3.3. Point Defects

Although single vacancies are hard to observe experimentally [45], they are easily tractable with DFT. It turns out that the investigated single vacancy lowers the adsorption strength in its direct adjacency with respect to the *pristine-like* graphene, as highlighted by the yellowish regions around the defect in Figure 3b. However, the region of influence is spatially very confined, since the adsorption energy values around second nearest neighboring hexagons already approach those of pristine graphene. Furthermore, Figure 3b suggests that the H₂ molecule is less likely to be adsorbed at those hexagons which are directly adjacent to the single vacancy defect, from an energetic point of view. Furthermore, there is no improvement of the minimum adsorption energy (Table 4), the lowest value occurs along the bonds to the hexagons adjacent to the defect.

Another very common point defect in hexagonal two-dimensional materials, and thus also observed experimentally [45,46], is a rotated bond which yields the Stone–Wales defect (Figure 3c). The highest value of the adsorption energy (i.e., the weakest physisorption) of the whole cell is predicted along the heptagon bonds, although the quantitative differences compared to the highest value in pristine graphene (see Table 4) are small ($\Delta E_{ads}^{max} \approx 2.5$ meV). Furthermore, we observe a narrow spatial confinement of the region with changed adsorption properties. Similarly to the vacancy, no qualitative improvement around the Stone–Wales defect can be observed as, e.g., there is no nearby region with improved adsorption behavior ($E_{ads} \leq \min(E_{ads,graphene})$). The only location with potentially improved adsorption are the hexagons adjacent to the pentagons, however, the quantitative improvement compared to pristine graphene (≈ 1.5 meV) is negligible. Interestingly the single vacancy defect weakens the minima in the adjacent hexagons, such that the surface area which lies around the graphene minimum (fourth and fifth column in Table 4) while it remains constant for the Stone–Wales defect, when comparing the values to those of pristine graphene. Nevertheless the comparison of the values of the single vacancy and Stone–Wales defect clearly shows a reduction of the adsorption capabilities.

Table 4. Summary of the adsorption characteristics: minimum and maximum values of adsorption maps for different scenarios (Figure 3, fraction of the surface (in the used supercell) with adsorption energy in the range of adsorption minimum of pristine graphene $E_{ads,graphene}^{min} + 1$ meV and $E_{ads,graphene}^{min} + 5$ meV, and fraction of the supercell area with adsorption energy lower than that of pristine graphene. The values of +1 meV and +5 meV, were chosen arbitrarily.

System	E_{ads} [meV]		Surface [%]		Increased Surface [%]
	min	max	$E_{ads,graphene}^{min} + 5$ meV	$E_{ads,graphene}^{min} + 1$ meV	$E_{ads,graphene}^{min}$
graphene	−68.7	−62.7	59.41	4.95	
single vacancy	−68.9	−59.6	32.02	1.47	0.14
Stone–Wales defect	−70.2	−59.1	46.88	4.93	1.43
(1,0) grain boundary	−72.6	−62.4	94.09	38.48	28.23
POP-graphene	−77.4	−64.2	100.00	71.39	49.91

3.4. Line Defects

Inspection of the last column of Table 4 reveals that point defects do not result in areas with lowered adsorption energy compared to pristine graphene. Moreover, the adsorption landscape is apparently more undulating as demonstrated by smaller fractions of the surface with adsorption energies close to the lowest adsorption energy. Such behaviour can even counteract physisorption, hence we continue with investigating other defects, namely the (1,0) grain boundary as a representative of line defects. This is still tractable with DFT with reasonable computational demands. Due to the periodic boundary conditions, the simulation cell contains two boundaries, whose cores are 11.33 Å apart. Figure 3e shows a clip around the grain boundary core which itself forms a *heptagon-pentagon-2 hexagon* line. The minima of adsorption are located in the centers of the hexagons neighboring with the pentagons. Furthermore, the blueish color of Figure 3e, indicating less spatial confinement of the

line defect, when compared to the point defects, is underpinned by the number from Table 4. For this defect already nearly one third of the area lies below the minimum graphene level.

3.5. Globally Modified Graphene

The adsorption maps of the (1, 0) symmetric tilt grain boundaries reveal that when measuring adsorption by the adsorption energy, a qualitative enhancement occurs around regions with pentagonal arrangement of the carbon atoms. A recently proposed globally modified graphene composed of ordered pentagons and octagons, POP-graphene, seems therefore a promising candidate for enhancing the H₂ adsorption. Indeed, our calculations predict very good adsorption behavior in the pentagons area (see Figure 3e), the absolute minimum is located in the center of the octagons. With an absolute value of -77.4 meV, this minimum is the strongest of all structures investigated in the present study. Consequently, the POP-graphene shows stronger adsorption throughout the whole super cell with $\approx 50\%$ of area exhibiting lower E_{ads} than $\min(E_{ads,graphene})$. Moreover, the highest absolute value of $\max(E_{ads,POP-graphene})$ (weakest adsorption) is just a few meV away from the minimum of pristine graphene $\approx \min(E_{ads,graphene}) + 4.5$ meV, resulting that the whole cell is lying below the 5 meV and over 70% of the surface below the 1 meV border respectively.

4. Discussion

In this section we try to analyze the origin of the improved adsorption of the POP-graphene as well as the apparent local adsorption enhancement caused by point defects (Figure 3). There are two possible sources: (1) change in the electron distribution within carbon-structure due to defects, that affects the polarizability; (2) pure geometry, i.e., arrangement of the C atoms. Inspecting Equation (1), the former contribution should mostly cancel out as it affects (by almost the same amount) both terms $E_{tot,graphene+H_2}$ and $E_{tot,graphene}$. Therefore, the change in adsorption behavior should be linked to the changed interaction between the molecule and the graphene structure which is mainly van-der-Waals-like. This can be demonstrated, e.g., by comparing the adsorption energies the *top-v* configuration with $E_{ads,graphene}^{top-v} = -62$ meV (Table 3) and without $E_{ads,graphene}^{top-v} = -12$ meV (pure GGA-PBE) TS correction, which agrees well with previously published data [40,42].

To bring more insight, we now analyze different contributions to the adsorption energy taking POP-graphene as an example. As the total interaction energies may be splitted up into a small PBE contribution and a dispersion part arising from the vdW corrections one can rewrite it to:

$$E_{int} = E_{int}^{PBE} + E_{disp} = \underbrace{E_{int}^{PBE} - \max(E_{int}^{PBE})}_{\Delta E_{int}^{PBE} - \text{Figure 4a}} + \underbrace{E_{disp} - \max(E_{disp})}_{\Delta E_{disp} - \text{Figure 4b}} + C = \Delta E_{int}^{PBE} + \Delta E_{disp} + C \quad (3)$$

where $C = \max(E_{int}^{PBE}) + \max(E_{disp})$ is a constant term throughout the whole simulation cell, and is found to be $C = -61.18$ meV for POP-graphene. Firstly, we extracted the “adsorption maps” for pure GGA-PBE without any vdW correction. These values are shown in Figure 4a as relative values with respect to the maximum value identified on the whole adsorption surface (ΔE_{int}^{PBE}). This way we hope to highlight the “topology” changes due to different levels of approximation. Most importantly, the adsorption surface for the pure GGA-PBE is rather flat with the difference between the maxima and minima being $\min(\Delta E_{int}^{PBE}) = -5.29$ meV with the minima (darkest regions) being located in the centres of the pentagons. This is clearly different from the vdW part of the adsorption energy (Figure 4c): the adsorption minima are located in the centres of octagons and their relative depth is $\min(\Delta E_{disp}) = -16.21$ meV. The adsorption surface maxima are located on the sides between octagons, same as in the case of the full adsorption surface (Figure 3e). Therefore, we ascribe the main origin of the adsorption maps topology to the vdW dispersion interaction.

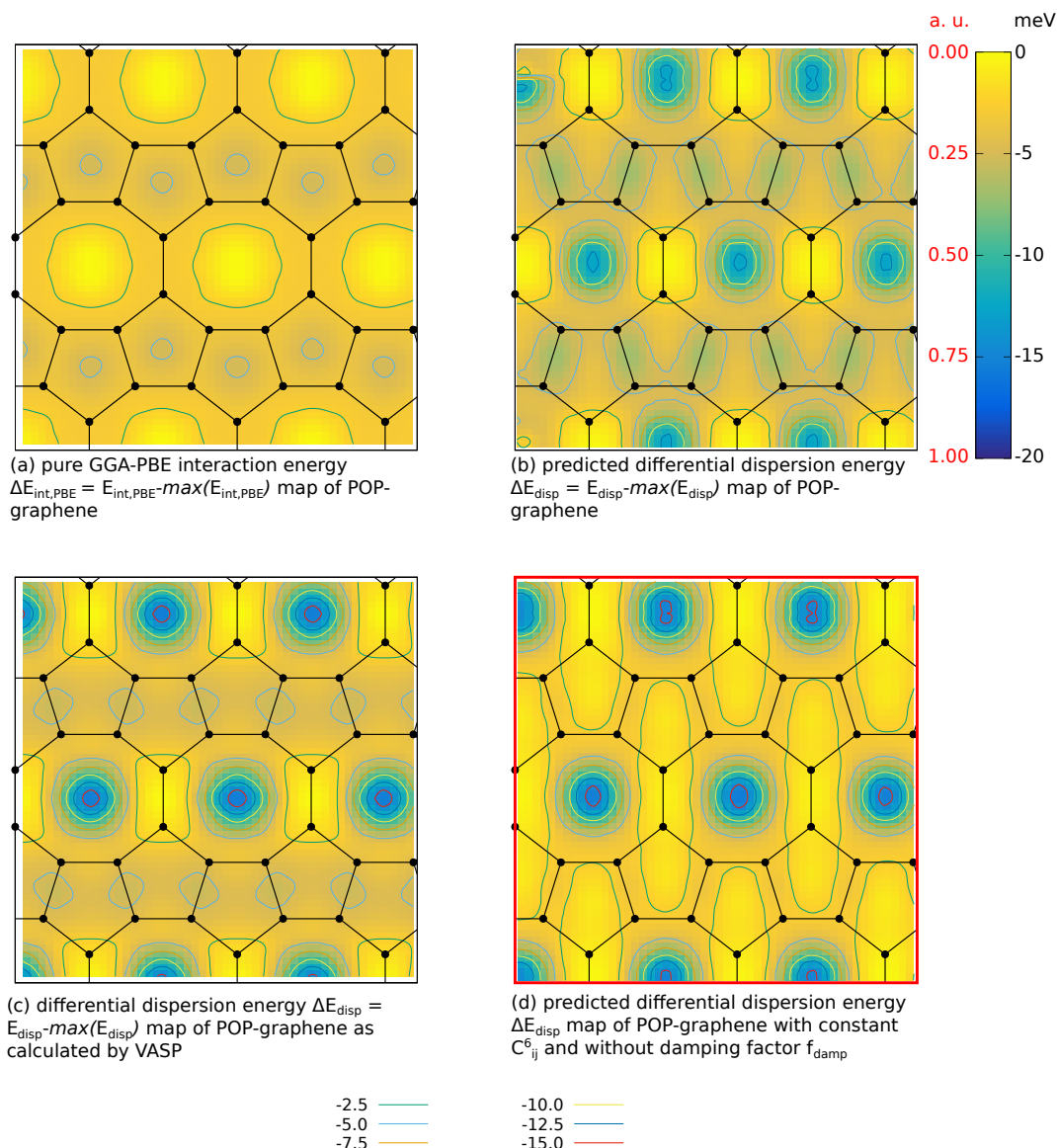


Figure 4. Contributions to the adsorption energy maps. (a) pure PBE-GGA energies, (b) analytical vdW dispersion according to Equations (4) and (5), (c) TS vdW dispersion calculated by VASP, and (d) geometry-dictated topology form the $\sum 1/r_{ij,L}$ term. The corresponding full adsorption energy map is in Figure 3e. Contour lines are plotted every 2.5 meV.

As the next step we calculated dispersion energy for a hydrogen molecule for each sampling point according to Grimme's D2 method [34].

$$E_{\text{disp}} = -\frac{1}{2} \sum_{i=1}^N \sum_{j=1}^N \sum_{\mathbf{L}} \frac{C_{6ij}}{r_{ij,L}^6} f_{d,6}(r_{ij,L}^6) \quad (4)$$

$$f_{d,6}(r_{ij,L}^6) = \frac{s_6}{1 + e^{-d(r_{ij}/(s_R R_{0ij}) - 1)}} \quad (5)$$

To keep things simple, only contributions (sum over \mathbf{L}) from neighboring cells were taken into account. The parameters for the damping function s_6 , d , s_R and R_{0ij} were chosen according to the recommendations in the VASP manual [47].

Moreover, since the present work employed the TS vdW method, which essentially differs by the way how the dispersion coefficients C_{6ij} are calculated (from the charge density instead of constants), the values were taken as calculated by VASP. Nonetheless, following the derivation in Ref. [24], it

is possible to show that the variation of the dispersion coefficients is expected to be negligible. The dispersion coefficients within the TS method are calculated according to the following equations:

$$\alpha_i = v_i a_i^{\text{free}}, \quad (6)$$

$$C_{6ii} = v_i^2 C_{6ii}^{\text{free}}, \quad (7)$$

$$C_{6ij} = \frac{2C_{6ii}^{\text{free}} C_{6jj}^{\text{free}}}{\frac{\alpha_j}{\alpha_i} C_{6ii}^{\text{free}} + \frac{\alpha_i}{\alpha_j} C_{6jj}^{\text{free}}}, \quad (8)$$

where α_i^{free} is the polarizability of an isolated atom i and C_{6ii} the dispersion coefficient for a pair of those atoms. Due to a assumption of a linear dependence between polarizability and effective volume [48] of the atom v_i (obtained by employing Hirshfeld partitioning [49]), the effective volume is the only quantity which is calculated from the charge-density in order to obtain the dispersion coefficients. Therefore, plugging Equations (6) and (7) into Equation (8) reveals the linear dependence between v_i and C_{6ij}

$$C_{6ij} = \frac{2C_{6ii}^{\text{free}} C_{6jj}^{\text{free}} \alpha_i^{\text{free}} \alpha_j^{\text{free}}}{\underbrace{C_{6ii}^{\text{free}} (\alpha_j^{\text{free}})^2 + C_{6jj}^{\text{free}} (\alpha_i^{\text{free}})^2}_{\text{constant}}} v_i v_j. \quad (9)$$

Here, α_i^{free} and C_{6ii}^{free} are the polarizability and dispersion coefficient of an isolated atoms i , respectively, and can be found tabulated [50]. The dispersion coefficients for the POP-graphene differ only in a range of $\approx 1.7\% \frac{|\max(C_{6ij}) - \min(C_{6ij})|}{\langle C_{6ij} \rangle}$, caused by only small variations $\frac{|\max(v) - \min(v)|}{\langle v \rangle} \approx 0.85\%$ of the effective volume. Consequently the contribution arising from the changed electronic structure is rather small.

Comparing Figure 4b (calculated according to Equations (4) and (5) Figure 4c (full TS-VASP dispersion) suggests that the essential contributions to the adsorption surface topology are captured by the analytical form of Equation (4). Here, the geometry enters two terms: on the one hand directly through the $1/r^6$ term, and secondly through the damping coefficient. Setting the dispersion as well as damping coefficients to a constant value, Equation (4) simplifies to

$$E_{\text{disp}} \propto - \sum_{i=1}^N \sum_{j=1}^N \sum_{\mathbf{L}} \frac{1}{r_{ij,\mathbf{L}}^6}. \quad (10)$$

Thus, in Figure 4d the topology corresponding to only the geometry of the POP-graphene is shown, as given by Equation (10) (minimum-to-maximum scaled to fit the colour bar of the other dispersion maps). Clearly, the adsorption features such as preferred adsorption sites are related simply to the geometrical arrangement of the atoms involved in evaluation of the van-der-Waals dispersion, the major contribution to the adsorption energy.

5. Conclusions

After showing that our DFT-TS study is in good agreement with previous work [4], we could show that point defects such as single vacancies and Stone–Wales defects weaken the H₂ adsorption in their closest neighbourhood, however, the effects remain spatially confined. On the contrary, the impact of a (1,0) grain boundary on the adsorption properties is widespread, thus showing superior absolute values and large regions with enhanced adsorption properties as compared with the pristine graphene. POP-graphene, an example of a graphene derivative, outperforms even the grain boundary in terms of the enhanced area and the adsorption energies (adsorption is stronger). Furthermore, we showed explicitly by analyzing the effective atom volumes of POP-graphene, that the influence of the electronic structure to the dispersion correction has only a negligible impact. Hence no qualitative differences

can be expected when employing the DFT-D3 method instead of the DFT-TS one, being also the reason for the aforementioned good agreement with previous literature on graphene. As a consequence, the changes in the adsorption capabilities mainly arise from the different geometrical arrangement of the carbon atoms in the investigated structures.

Author Contributions: Conceptualization, D.G. and D.H.; methodology, D.G.; validation, D.G., M.N.P. and D.H.; investigation, D.G. and T.D.; resources, D.H.; writing—original draft preparation, D.G.; writing—review and editing, D.H., M.N.P. and T.D.; visualization, D.G.; supervision, D.H.; funding acquisition, M.N.P. and D.H. All authors have read and agree to the published version of the manuscript.

Funding: The author gratefully acknowledges the financial support under the scope of the COMET program within the K2 Center “Integrated Computational Material, Process and Product Engineering (IC-MPPE)” (Project No. 859480). This program is supported by the Austrian Federal Ministries for Transport, Innovation and Technology (BMVIT) and for Digital and Economic Affairs (BMDW), represented by the Austrian research funding association (FFG), and the federal states of Styria, Upper Austria and Tyrol.

Acknowledgments: The computational results presented have been achieved (in part) using the Vienna Scientific Cluster 3 (VSC-3).

Conflicts of Interest: The authors declare no conflict of interest.

Appendix A. Benchmark Study of Different van-der-Waals Corrections in VASP

Table A1. Benchmark study of different van-der-Waals corrections implemented in VASP in order to reproduce the experimental lattice parameters of graphite. (D2 = DFT-D2, D3 = DFT-D3, D3-BJ = DFT-D3 with *Becke-Jonson* (rational) damping, TS = Tkatchenko-Scheffler method, TS+IHiPart = Tkatchenko-Scheffler method with iterative *Hirshfeld* partitioning, MBD=Many-body dispersion energy method (MBD@rSC), dDsC = density-dependent-dispersion-correction method). IVDW refers to the setting of the van-der-Waals-method correction tag in the VASP control input file (INCAR). The last two rows show the deviation norm as well as the percentage norm. A Γ -centered $25 \times 25 \times 10$ k -mesh was used in combination very fine FFT-grid was used (increased setting for NGXF, NGYF, NGZF parameters, and a cut-off energy of 1100 eV) in order to get accurate energies and forces.

Method	Unit	None	D2	D3	D3-BJ	TS	TS+IHiPart	MBD	dDsC
IVDW		0	10	11	12	20	21	202	4
$c_{\text{exp}} = 6.708 \text{ \AA}$									
c_{calc}	\AA	7.978	6.447	6.952	6.709	6.708	6.710	6.743	6.707
$ c_{\text{exp}} - c_{\text{calc}} $	\AA	1.270	0.261	0.244	0.001	0.000	0.002	0.035	0.001
$ c_{\text{exp}} - c_{\text{calc}} /c_{\text{exp}}$	%	18.933	3.891	3.637	0.015	0.000	0.030	0.522	0.015
$a_{\text{exp}} = 2.461 \text{ \AA}$									
a_{calc}	\AA	2.467	2.463	2.466	2.466	2.460	2.460	2.461	2.455
$ a_{\text{exp}} - a_{\text{calc}} $	\AA	0.006	0.002	0.005	0.005	0.001	0.001	0.000	0.006
$ a_{\text{exp}} - a_{\text{calc}} /a_{\text{exp}}$	%	0.244	0.081	0.203	0.203	0.041	0.041	0.000	0.244
$\sqrt{ a_{\text{exp}} - a_{\text{calc}} ^2 + c_{\text{exp}} - c_{\text{calc}} ^2}$	\AA	1.270	0.261	0.244	0.005	0.001	0.002	0.035	0.006
$\sqrt{\left \frac{a_{\text{exp}} - a_{\text{calc}}}{a_{\text{exp}}}\right ^2 + \left \frac{c_{\text{exp}} - c_{\text{calc}}}{c_{\text{exp}}}\right ^2}$	%	18.934	3.892	3.643	0.204	0.041	0.050	0.522	0.244

Appendix B. Adsorption POP-graphene

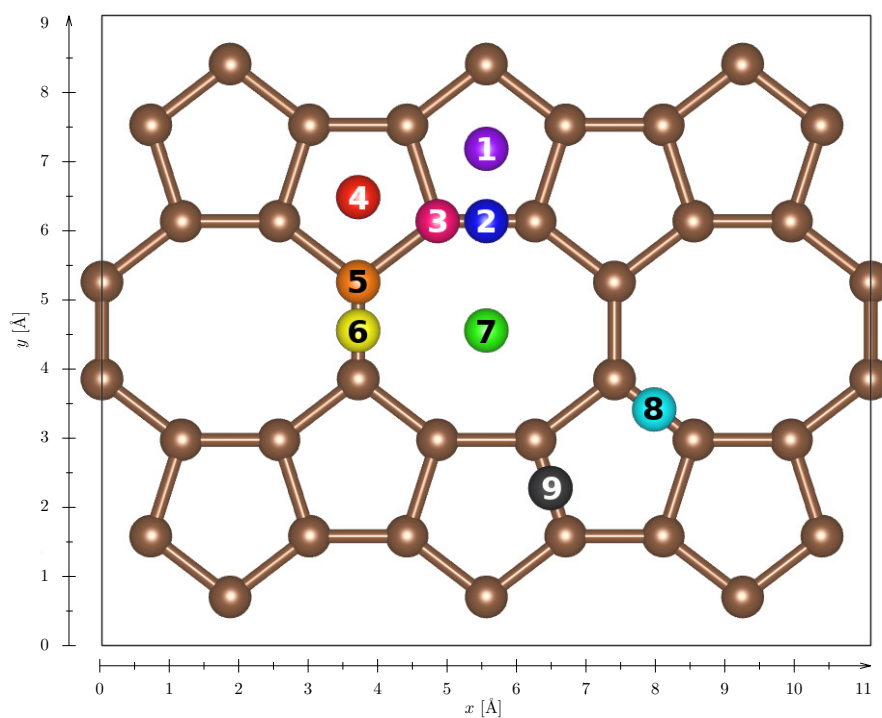


Figure A1. Schematic view of adsorption sites on POP-graphene. The colored balls represent the adsorption sites, where the number inside represents the sites' index. The interaction energies $E_{int,POP-graphene+H_2}^{(1)-(9)}$ were calculated for all three (x, y and z) alignments of the H_2 molecule axis. The data is presented in Figure A2.

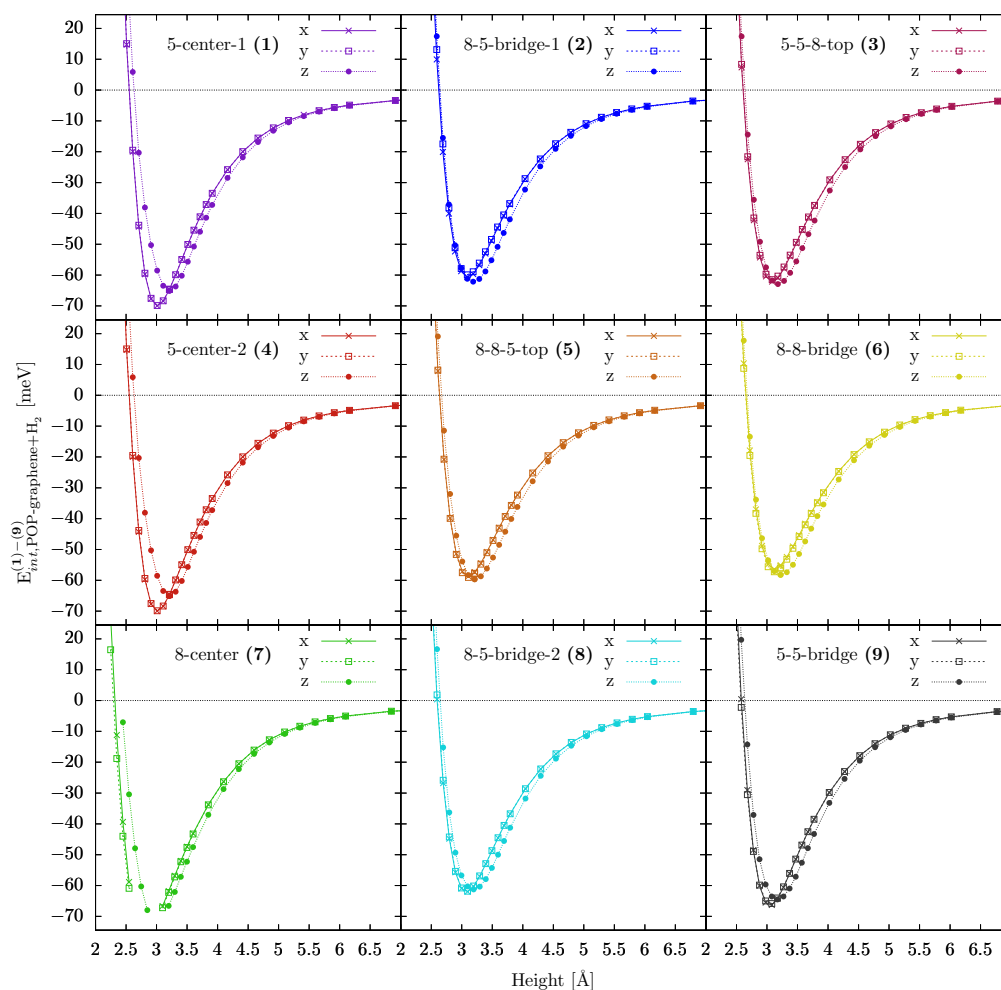


Figure A2. Interaction energies $E_{int,POP-graphene+H_2}^{(1)-(9)}$ for (x,y and z) alignment of the H_2 molecule on POP-graphene (as shown in Figure A1). The colors of the the balls in Figure A1, labelling special positions, corresponds width the colors of the curves. The numbers in the figure titles represents the corresponding carbon structure (5=pentagon, 8=octagon), e.g., 8-8-bridge is bond between two adjacent octagons.

References

1. Bastos-Neto, M.; Patzschke, C.; Lange, M.; Möllmer, J.; Möller, A.; Fichtner, S.; Schrage, C.; Lässig, D.; Lincke, J.; Staudt, R.; et al. Assessment of hydrogen storage by physisorption in porous materials. *Energy Environ. Sci.* **2012**, *5*, 8294–8303. [[CrossRef](#)]
2. Novoselov, K.S. Electric Field Effect in Atomically Thin Carbon Films. *Science* **2004**, *306*, 666–669. [[CrossRef](#)] [[PubMed](#)]
3. Geim, A.K.; Novoselov, K.S. The rise of graphene. *Nat. Mater.* **2007**, *6*, 183–191. [[CrossRef](#)] [[PubMed](#)]
4. Petrushenko, I.K.; Petrushenko, K.B. Hydrogen adsorption on graphene, hexagonal boron nitride, and graphene-like boron nitride-carbon heterostructures: A comparative theoretical study. *Int. J. Hydrogen Energy* **2018**, *43*, 801–808. [[CrossRef](#)]
5. Mattera, L.; Rosatelli, F.; Salvo, C.; Tommasini, F.; Valbusa, U.; Vidali, G. Selective adsorption of $1H_2$ and $2H_2$ on the (0001) graphite surface. *Surf. Sci.* **1980**, *93*, 515–525. [[CrossRef](#)]
6. Rangel, E.; Sansores, E. Theoretical study of hydrogen adsorption on nitrogen doped graphene decorated with palladium clusters. *Int. J. Hydrogen Energy* **2014**, *39*, 6558–6566. [[CrossRef](#)]

7. Nguyen, M.T. Reactivity of Graphene and Hexagonal Boron Nitride In-Plane Heterostructures with Oxygen: A DFT Study. *ChemPhysChem* **2014**, *15*, 2372–2376. [[CrossRef](#)]
8. Petrushenko, I.K. A DFT Study of Hydrogen Adsorption onto Graphene: Effect of Nitrogen Doping. *J. Nano-Electron. Phys.* **2017**, *9*, 03018–1–03018–5. [[CrossRef](#)]
9. Gadipelli, S.; Guo, Z.X. Graphene-based materials: Synthesis and gas sorption, storage and separation. *Prog. Mater. Sci.* **2015**, *69*, 1–60. [[CrossRef](#)]
10. Bakhshi, F.; Farhadian, N. Co-doped graphene sheets as a novel adsorbent for hydrogen storage: DFT and DFT-D3 correction dispersion study. *Int. J. Hydrogen Energy* **2018**, *43*, 8355–8364. [[CrossRef](#)]
11. Holec, D.; Kostoglou, N.; Tampaxis, C.; Babic, B.; Mitterer, C.; Rebholz, C. Theory-guided metal-decoration of nanoporous carbon for hydrogen storage applications. *Surf. Coat. Technol.* **2018**, *351*, 42–49. [[CrossRef](#)]
12. Samantaray, S.S.; Sangeetha, V.; Abinaya, S.; Ramaprabhu, S. Enhanced hydrogen storage performance in Pd3Co decorated nitrogen/boron doped graphene composites. *Int. J. Hydrogen Energy* **2018**, *43*, 8018–8025. [[CrossRef](#)]
13. Wu, D.; Yang, B.; Ruckenstein, E.; Chen, H. Functionalization: An Effective Approach to Open and Close Channels for Electron Transfer in Nitrogenated Holey Graphene C2N Anodes in Sodium-Ion Batteries. *J. Phys. Chem. Lett.* **2019**, *10*, 721–726. [[CrossRef](#)] [[PubMed](#)]
14. Baburin, I.A.; Klechikov, A.; Mercier, G.; Talyzin, A.; Seifert, G. Hydrogen adsorption by perforated graphene. *Int. J. Hydrogen Energy* **2015**, *40*, 6594–6599. [[CrossRef](#)]
15. Wang, S.; Yang, B.; Chen, H.; Ruckenstein, E. Reconfiguring graphene for high-performance metal-ion battery anodes. *Energy Storage Mater.* **2019**, *16*, 619–624. [[CrossRef](#)]
16. Stone, A.; Wales, D. Theoretical studies of icosahedral C60 and some related species. *Chem. Phys. Lett.* **1986**, *128*, 501–503. [[CrossRef](#)]
17. Thrower, P. The study of defects in graphite by transmission electron microscopy. *Chem. Phys. Carbon* **1969**, *5*, 217–320.
18. Yazyev, O.V.; Louie, S.G. Topological defects in graphene: Dislocations and grain boundaries. *Phys. Rev. B* **2010**, *81*, 195420. [[CrossRef](#)]
19. Liu, T.H.; Gajewski, G.; Pao, C.W.; Chang, C.C. Structure, energy, and structural transformations of graphene grain boundaries from atomistic simulations. *Carbon* **2011**, *49*, 2306–2317. [[CrossRef](#)]
20. Lusk, M.T.; Carr, L. Creation of graphene allotropes using patterned defects. *Carbon* **2009**, *47*, 2226–2232. [[CrossRef](#)]
21. Liu, Y.; Yakobson, B.I. Cones, Pringles, and Grain Boundary Landscapes in Graphene Topology. *Nano Lett.* **2010**, *10*, 2178–2183. [[CrossRef](#)]
22. Ariza, M.; Ortiz, M. Discrete dislocations in graphene. *J. Mech. Phys. Solids* **2010**, *58*, 710–734. [[CrossRef](#)]
23. Wang, S.; Yang, B.; Chen, H.; Ruckenstein, E. Popgraphene: A new 2D planar carbon allotrope composed of 5–8–5 carbon rings for high-performance lithium-ion battery anodes from bottom-up programming. *J. Mater. Chem. A* **2018**, *6*, 6815–6821. [[CrossRef](#)]
24. Tkatchenko, A.; Scheffler, M. Accurate molecular van der Waals interactions from ground-state electron density and free-atom reference data. *Phys. Rev. Lett.* **2009**, *102*, 6–9. [[CrossRef](#)] [[PubMed](#)]
25. Ong, S.P.; Richards, W.D.; Jain, A.; Hautier, G.; Kocher, M.; Cholia, S.; Gunter, D.; Chevrier, V.L.; Persson, K.A.; Ceder, G. Python Materials Genomics (pymatgen): A robust, open-source python library for materials analysis. *Comput. Mater. Sci.* **2013**, *68*, 314–319. [[CrossRef](#)]
26. Oliphant, T. E.; Python for Scientific Computing. *Comput. Sci. Eng.* **2007**, *9*, 10–20, doi.org/10.1109/mcse.2007.58. [[CrossRef](#)]
27. Kresse, G.; Hafner, J. Ab initio molecular dynamics for liquid metals. *Phys. Rev. B* **1993**, *47*, 558–561. [[CrossRef](#)]
28. Kresse, G.; Furthmüller, J. Efficient iterative schemes for ab initio total-energy calculations using a plane-wave basis set. *Phys. Rev. B* **1996**, *54*, 11169–11186. [[CrossRef](#)]
29. Perdew, J.P.; Ernzerhof, M.; Burke, K. Generalized Gradient Approximation Made Simple. *Phys. Rev. Lett.* **1996**, *77*, 3865–3868. [[CrossRef](#)]
30. Perdew, J.P.; Burke, K.; Ernzerhof, M. Generalized Gradient Approximation Made Simple. *Phys. Rev. Lett.* **1997**, *78*, 1396. [[CrossRef](#)]
31. Blöchl, P.E. Projector augmented-wave method. *Phys. Rev. B* **1994**, *50*, 17953–17979. [[CrossRef](#)]

32. Kresse, G.; Joubert, D. From ultrasoft pseudopotentials to the projector augmented-wave method. *Phys. Rev. B* **1999**, *59*, 1758–1775. [[CrossRef](#)]
33. Monkhorst, H.J.; Pack, J.D. Special points for Brillouin-zone integrations. *Phys. Rev. B* **1976**, *13*, 5188–5192. [[CrossRef](#)]
34. Grimme, S. Accurate description of van der Waals complexes by density functional theory including empirical corrections. *J. Comput. Chem.* **2004**, *25*, 1463–1473. [[CrossRef](#)] [[PubMed](#)]
35. Grimme, S.; Antony, J.; Ehrlich, S.; Krieg, H. A consistent and accurate ab initio parametrization of density functional dispersion correction (DFT-D) for the 94 elements H-Pu. *J. Chem. Phys.* **2010**, *132*. [[CrossRef](#)] [[PubMed](#)]
36. Tkatchenko, A.; Distasio, R.A.; Car, R.; Scheffler, M. Accurate and efficient method for many-body van der Waals interactions. *Phys. Rev. Lett.* **2012**, *108*, 1–5. [[CrossRef](#)]
37. Bučko, T.; Lebègue, S.; Hafner, J.; Ángyán, J.G. Improved density dependent correction for the description of London dispersion forces. *J. Chem. Theory Comput.* **2013**, *9*, 4293–4299. [[CrossRef](#)]
38. Bučko, T.; Lebègue, S.; Hafner, J.; Ángyán, J.G. Tkatchenko-Scheffler van der Waals correction method with and without self-consistent screening applied to solids. *Phys. Rev. B* **2013**, *87*. [[CrossRef](#)]
39. Al-Saidi, W.A.; Voora, V.K.; Jordan, K.D. An Assessment of the vdW-TS Method for Extended Systems. *J. Chem. Theory Comput.* **2012**, *8*, 1503–1513. [[CrossRef](#)]
40. Rubes, M.; Bludsky, O. DFT/CCSD(T) Investigation of the Interaction of Molecular Hydrogen with Carbon Nanostructures. *ChemPhysChem* **2009**, *10*, 1868–1873. [[CrossRef](#)]
41. Okamoto, Y.; Miyamoto, Y. Ab Initio Investigation of Physisorption of Molecular Hydrogen on Planar and Curved Graphenes. *J. Phys. Chem. B* **2001**, *105*, 3470–3474. [[CrossRef](#)]
42. Krishnan, S.; Vadapoo, R.; Riley, K.E.; Velez, J.P. Dispersion-corrected density functional theory comparison of hydrogen adsorption on boron-nitride and carbon nanotubes. *Phys. Rev. B* **2011**, *84*. [[CrossRef](#)]
43. Matanović, I.; Belof, J.L.; Space, B.; Sillar, K.; Sauer, J.; Eckert, J.; Bačić, Z. Hydrogen adsorbed in a metal organic framework-5: Coupled translation-rotation eigenstates from quantum five-dimensional calculations. *J. Chem. Phys.* **2012**, *137*, 014701. [[CrossRef](#)] [[PubMed](#)]
44. Ganji, M.D.; Hosseini-khah, S.M.; Amini-tabar, Z. Theoretical insight into hydrogen adsorption onto graphene: A first-principles B3LYP-D3 study. *Phys. Chem. Chem. Phys.* **2015**, *17*, 2504–2511. [[CrossRef](#)] [[PubMed](#)]
45. Björkman, T.; Kurasch, S.; Lehtinen, O.; Kotakoski, J.; Yazyev, O.V.; Srivastava, A.; Skakalova, V.; Smet, J.H.; Kaiser, U.; Krasheninnikov, A.V. Defects in bilayer silica and graphene: Common trends in diverse hexagonal two-dimensional systems. *Sci. Rep.* **2013**, *3*. [[CrossRef](#)]
46. Kotakoski, J.; Meyer, J.C.; Kurasch, S.; Santos-Cottin, D.; Kaiser, U.; Krasheninnikov, A.V. Stone–Wales-type transformations in carbon nanostructures driven by electron irradiation. *Phys. Rev. B* **2011**, *83*. [[CrossRef](#)]
47. Kresse, G.; Furthmüller, J.; Marsman, M. *The VASP Manual - Vaspwiki*. Available online: https://www.vasp.at/wiki/index.php/The_VASP_Manual (accessed on 23 March 2020).
48. Brinck, T.; Murray, J.S.; Politzer, P. Polarizability and volume. *J. Chem. Phys.* **1993**, *98*, 4305–4306. [[CrossRef](#)]
49. Hirshfeld, F.L. Bonded-atom fragments for describing molecular charge densities. *Theor. Chim. Acta* **1977**, *44*, 129–138. [[CrossRef](#)]
50. Chu, X.; Dalgarno, A. Linear response time-dependent density functional theory for van der Waals coefficients. *J. Chem. Phys.* **2004**, *121*, 4083–4088. [[CrossRef](#)]

